Separation and Purification Technology 272 (2021) 118896

Contents lists available at ScienceDirect

Separation and Purification Technology

journal homepage: www.elsevier.com/locate/seppur

Synthesis of noble metal-decorated NH_2-MIL-125 titanium MOF for the photocatalytic degradation of acetaminophen under solar irradiation

V. Muelas-Ramos, C. Belver, J.J. Rodriguez, J. Bedia *

Chemical Engineering Department, Universidad Autónoma de Madrid, Campus Cantoblanco, E-28049 Madrid, Spain

ARTICLE INFO

Keywords:
NH_2-MIL-125
Noble metal nanoparticles
Photocatalysis
Acetaminophen
Water treatment

ABSTRACT

This work reports the solvothermal synthesis of a titanium-based metal organic framework (NH_2-MIL-125(Ti)) and the further deposition of palladium, platinum and silver nanoparticles on its framework, with the aim to obtain visible light-driven photocatalysts. The structure of the NH_2-MIL-125 was not affected by the incorporation of the metal nanoparticles, while the textural properties changed depending on the metal used. All M/NH_2-MIL-125 (M = Pd, Pt, Ag) synthesized materials showed enhanced light absorption in the visible region due to the effect of the metal nanoparticles, which were mainly in reduced state as confirmed by XPS analyses. The metal nanoparticles were between 1.8 and 3.8 nm in size depending of the metal. They were responsible for the reduction in the recombination process, as suggested by photoluminescence measurements. The photocatalytic performance of M/NH_2-MIL-125 was tested for the degradation of acetaminophen (ACE) under simulated solar irradiation. Pt/NH_2-MIL-125 achieved the highest conversion rate (rate constant of 0.0165 min^{-1}), with complete conversion of the contaminant in less than three hours. Scavengers studies confirmed that $O_2^{\bullet-}$ radicals play a main role in the degradation process, followed by $^{\bullet}OH$ radicals. The catalytic stability of Pt/NH_2-MIL-125 was confirmed upon three successive reaction cycles. Different water matrices were tested to understand the effect of common inorganic ions, being the presence of bicarbonates the most detrimental to the performance of the photocatalytic process.

1. Introduction

The availability of quality water is a growing concern in current society. Thus, different purification technologies are worldwide investigated and implemented in the field of water and wastewater treatment. A new group of contaminants, which are not readily removed by conventional technologies, are of growing concern. This so-called emerging contaminants (ECs) include a wide range of pharmaceuticals, personal care products, detergents, steroids, hormones, etc. [1]. The concentration of ECs in water is in general fairly low, but even at these low levels they are hazardous for human health and environment, hence the importance of their effective removal [2]. Different wastewater treatment technologies are being considered for that purpose, being advanced oxidation processes (AOPs) promising solutions due to their ability to generate reactive oxygen species (ROS) capable of degrading a wide variety of contaminants. AOPs include different approaches, such as Fenton, ozonation, sonolysis, electrolysis and photocatalysis [3]. This last is receiving growing attention, especially regarding potential application under solar light [4]. Photocatalysis exploits the ability of a semiconductor to induce redox reactions when activated by light, being TiO_2 the most widely used photocatalyst since Fujishima and Honda discovered its properties [5]. TiO_2 presents unquestionable advantages, such as high-photoactivity and stability, low-toxicity and low-cost [6]. But, it has also some drawbacks, including a deficient exploitation of solar energy, since it only uses the UV radiation from the solar spectrum. Also, the fast recombination of electron-hole pairs and difficult recovery and recycling from the aqueous medium because of the very low particle size, limit the application of this material as photocatalyst [7]. Thus, other semiconductors have gained attention in this field to, especially for the sake of more efficient use of free solar irradiation as energy source.

Metal organic frameworks (MOFs) represent an interesting class of porous materials formed by the combination of a metal oxo-cluster and an organic linker [8]. They have been applied in many fields, such as gas storage [9,10], water splitting [11,12], sensing [13], separation processes [14,15], catalysts in green chemistry [16], and water treatment [17,18]. Regarding water purification, MOFs and derived-MOFs materials have been evaluated as promising photocatalysts due to their

* Corresponding author.
E-mail address: jorge.bedia@uam.es (J. Bedia).

https://doi.org/10.1016/j.seppur.2021.118896
Received 26 January 2021; Received in revised form 30 April 2021; Accepted 1 May 2021
Available online 11 May 2021
1383-5866/© 2021 The Author(s). Published by Elsevier B.V. This is an open access article under the CC BY-NC-ND license (http://creativecommons.org/licenses/by-nc-nd/4.0/).

semiconductor properties [19]. Among the different MOFs that can be synthesized by varying the metal and linker nature, Ti-MOFs are receiving great attention in photocatalysis. For instance, Dan-Hardi et al. [20] synthetized MIL-125, formed by $Ti_8O_8(OH)_4$ clusters and six coordinated linkers with very interesting photochemical properties and thermal stability. However, this MOF has a high band gap value, close to 3.6 eV, so that to be activated needs UV light. To overcome this problem, MIL-125 has been modified to enhance its photocatalytic activity by different methods, including ligand functionalization [21] metal cluster doping [22] metal sensitization [23,24] or combination with other semiconductors [25–27]. Regarding functionalization, modifying the ligand by the incorporation of a $—NH_2$ group results in NH_2-MIL-125 MOF, which has a significantly lower band gap value, close to 2.6 eV [21,28]. The $—NH_2$ functionalization and metal doping were simultaneously performed by Gómez-Avilés et al. [22] giving rise to (Ti/Zr)—NH_2-MIL-125, capable of removing acetaminophen from water in a short time under simulated solar light, where superoxide radicals were the main specie involved in the process. Among composites or heterostructures derived from MIL-125, In_2S_3@MIL-125 stands out for its efficiency in tetracycline breakdown under visible light again with superoxide radicals as main reactive specie in the degradation [29]. The aforementioned antibiotic, was also degraded with TiO_2@NH_2-MIL-125 under visible light irradiation [30]. Recently BiOI/MIL-125 heterojunction was employed to remove tetracycline, being holes the main reactive specie [31]. Moreover, another antibiotic, such as oxytetracycline was also removed using CdS@NH_2-MIL-125 [32]. MIL-125 was also combined with Bi_2WO_6 to remove tetracycline hydrochloride under visible light irradiation [33]. In this latter study, superoxide radicals and holes were identified as the main active species. A novel photocatalyst based on MIL-125 with mixed linkers was combined with different contents of g-C_3N_4 for the photodegradation of cefixime with a main participation in the degradation of superoxide radicals [34].

For instance, Pd and Ag were deposited on NH_2-MIL-125 to reduce nitro-aromatic compounds under visible light [35] attributing the better photocatalytic response to inhibition of the electron recombination due to the presence of metal nanoparticles. Pt NPs were used to improve its photocatalytic CO_2 reduction, since the metal nanoparticles reduce Ti^{4+} to Ti^{3+}, which is more active for CO_2 reduction [36] and also studied for H_2 photocatalytic production, where the metal NPs improve the charge separation [37]. Ag NPs deposition has been also investigated for the improvement of a modified NH_2-MIL-125 activity in the photocatalytic degradation of a dye under visible light, giving rise a better photodegradation owning to the plasmon resonance effect [23]. However, to the best of our knowledge, only one previous study is devoted to Pt-deposited NH_2-MIL-125 for water treatment (Cr(VI) reduction) by solar photocatalysis. In this study, the improvement in the photoactivity is associated to a faster electron transfer and lower recombination of electron-hole pairs [38].

The current work focusses the attention on the photocatalytic behavior of NH_2-MIL-125 with deposited noble metal NPs on its surface. These materials are tested as photocatalysts for the removal of acetaminophen (as model emerging pollutant) under simulated solar light. To the best of our knowledge, this is the first study that uses noble metal decorated NH_2-MIL-125 for the solar photocatalytic degradation of a contaminant of emerging concern such as acetaminophen. We performed a systematic characterization of the synthesized materials, studying the effect of the metal NPs on the photocatalytic activity. The acetaminophen degradation was studied in detail, determining the role of the main radicals involved in the reaction, analyzing the influence of some inorganic ions commonly present in water and stablishing the stability of the photocatalyst upon successive cycles. The study highlights the great activity of M/NH_2-MIL-125 for the removal of acetaminophen in water under solar light, providing useful information for future water treatment applications of MOFs.

2. Experimental

2.1. Synthesis of NH_2-MIL-125(Ti)

NH_2-MIL-125(Ti) was synthesized following previously reported procedures [22,39]. Briefly, 6 mmol of 2-amino benzene dicarboxylic acid (Sigma-Aldrich, 99%) were dissolved in 25 mL of N,N-dimethylformamide (DMF, Sigma-Aldrich, ≥99.8%) by stirring at room temperature for 5 min. Then, 3 mmol of titanium isopropoxide (Sigma-Aldrich, ≥97%) were added dropwise, until complete homogenization, followed by 25 mL of methanol (Sigma-Aldrich, 99.8%), maintaining the final mixture under stirring for 30 min. The solution was further transferred to a 65 mL Teflon-lined stainless steel autoclave and heated at 150 °C for 16 h. The resulting solid was centrifuged (5000 rpm, 5 min) and washed three times with DMF and other three times with methanol (100 mL each time for 30 min). The final yellow solid was recovered by centrifugation, dried at 60 °C overnight and stored. This sample is named NH_2-MIL-125.

2.2. Deposition of Pd and Pt NPs

Pd and Pt/NH_2-MIL-125 (1 wt%, Pt or Pd) were prepared by incipient wetness impregnation. Metal impregnation was carried out over the as-prepared NH_2-MIL-125 using an aqueous solution of $PdCl_2$ (Sigma-Aldrich, 99%) or H_2PtCl_6 (8 wt% in H_2O, Sigma-Aldrich, 99%).The impregnated samples were dried overnight in an oven at 60 °C and reduced under 25 mL·min^{-1} H_2 flow at 200 °C during 2 h. These modified-MOFs were denoted as Pd/NH_2-MIL-125 and Pt/NH_2-MIL-125.

2.3. Deposition of Ag NPs

Ag/NH_2-MIL-125 was prepared by photo-deposition of silver NPs [40]. The appropriate amount of NH_2-MIL-125 to achieve 1 wt% of Ag was added to 50 mL of 0.001 $AgNO_3$ (Alfa Aesar, 99%) ethanol solution under magnetic stirring for 30 min. Further, the suspension was irradiated at 25 °C with a commercial UV lamp (Ultra Vitalux 300 W) for 1 h under stirring. The solvent was removed by a rotary evaporator and the resulting solid was dried overnight at 60 °C.

2.4. Characterization

The Solid-State X-Ray Diffraction (XRD) patterns were registered in a Bruker D8 diffractometer equipped with a Sol-X energy dispersive detector, using a Cu Kα source (λ = 0.154 nm) and a 2θ range from 2 to 50° (scan step 1.5°·min^{-1}). The average crystal size (D) was calculated by the Scherreŕs equation, using the (2 1 1) peak at 11.6° of 2θ, that does not overlap with others. A TriStar 123 equipment (Micromeritics) was used to assess the porous texture by N_2 adsorption–desorption at −196 °C. The samples were previously outgassed under vacuum at 120 °C. The Brunauer-Emmet-Teller method [41] was used to calculate the specific surface area (S_{BET}). Total pore volume (V_T) was determined by the amount of N_2 adsorbed at 0.99 relative pressure (P/P_0). Micropore volume (V_{MP}) was obtained from the t-plot method [42]. The pore size distribution was determined by the density functional theory (DFT) model. UV–visible diffuse reflectance spectra were registered with a Shimadzu 2501PC UV–vis spectrophotometer in the 200–800 nm range, using $BaSO_4$ as reference. The band gap values were calculated from those spectra by the Tauc Plot method [28,43], considering all materials as indirect semiconductors [44]. The surface composition was analysed by X-ray photoelectron spectroscopy (XPS) with a Thermo Scientific apparatus using Al Kα radiation (1486.68 eV). All binding energies were corrected using as reference the C 1s spectrum at 284.6 eV. The binding energy was taken from 0 to 1200 eV. Scanning transmission electron microscopy (STEM) images were obtained with an Analytical Titan apparatus (CEOS Co.). Chemical analyses of the solids were carried out by inductively coupled plasma mass spectrometry (ICP-MS) in a NexION

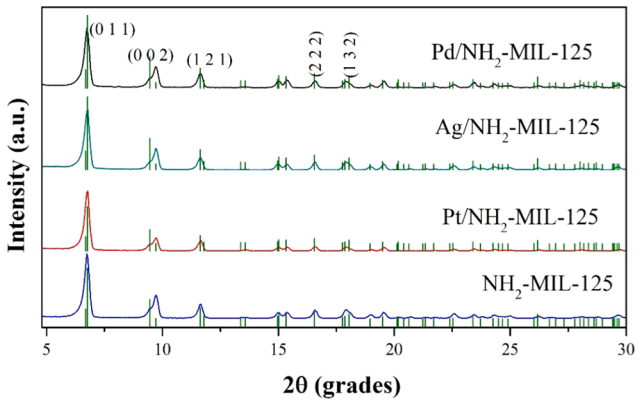

Fig. 1. X-ray diffraction patterns. Reference pattern of NH_2-MIL-125 from Crystal Open Database (COD) library is included in green colour (COD-7211159.cif [52]).

300 instrument. Prior to the analysis the solids were digested in acid medium and stabilize with HF. A Cary Eclipse spectrofluorometer was used to obtain the photoluminescence (PL) spectra, using an excitation wavelength of 370 nm.

2.5. Photocatalytic tests

Photodegradation of acetaminophen (ACE, Sigma-Aldrich, >99%) was undertaken in a circular Pyrex jacketed reactor (500 mL) (radius = 9.84 cm; height = 7.15 cm) at a controlled temperature of 25 °C under magnetic stirring. This reactor was located inside a solar simulator chamber (Suntest XLS+, ATLAS) with a Xe lamp and a "Daylight" filter (cuts off $\lambda \leq 290$ nm, emission spectrum shown in Fig. S1). The light intensity was fixed to 600 $W \cdot m^{-2}$ (107.14 klx). The photocatalyst (250 $mg \cdot L^{-1}$) was suspended in 150 mL aqueous solution with an initial ACE concentration of 5 $mg \cdot L^{-1}$. Adsorption equilibrium was achieved in dark for 1 h prior to the photocatalytic reaction. Then, the light was switched on and the reaction was followed for 6 h. Aliquots were taken at given time intervals and filtered with PTFE syringeless filters (Whatman 0.2 μm) to separate the solid photocatalyst. The ACE concentration was analysed by liquid chromatography HPLC (Shimadzu Prominence-I LC-2030C) using a diode array detector (SPD-M30A) and a C18 column (Eclipse Plus 5 μm, Agilent). The mobile phase was a mixture of acetonitrile/acetic acid (0.1% v/v aqueous solution), using a gradient 10/90–40/60% method (0.7 $mL \cdot min^{-1}$). The detection wavelength was fixed at the maximum absorption of ACE, 246 nm. Radical trapping experiments were carried out with benzoquinone (BQ) as scavenger for superoxide radicals ($O_2^{\cdot-}$) [45], isopropanol (IPA) for hydroxyl radicals ($^{\cdot}OH$) [46], silver nitrate for holes (h^+) [47] and potassium iodide (KI) as electron (e^-) acceptor [48]. These experiments were performed under the same conditions than the reaction ones, adding the scavenger at 1 mM initial concentration to the ACE solution [49] after the dark adsorption equilibrium step. The effect of some inorganic ions commonly present in water was also studied. These tests were carried out with Cl^- (25 $mg \cdot L^{-1}$), NO_3^- (50 $mg \cdot L^{-1}$), SO_4^{2-} (50 $mg \cdot L^{-1}$) and HCO_3^- (150 $mg \cdot L^{-1}$), usual values in real waters. The stability of the photocatalyst was evaluated upon three successive cycles. After each cycle, the photocatalyst was vacuum-filtered, washed three with 300 mL of distilled water, dried at 60 °C overnight and weighed, ensuring that the reaction conditions of the following cycle were the same.

Reaction intermediates were analyzed by Liquid Chromatography Mass Spectrometry with Electrospray Ionization (LC/ESI-MS) in a Bruker Maxis II equipment using a positive ionization mode. It was employed a 500 V end plate offset, at 300 °C, a 3.500 V capillary voltage and 8 $mL \cdot min^{-1}$ of dry gas flow. The data were collected in the range of 50–3000 *m/z*. A Metrohm 790 IC apparatus, equipped with a Metrosep A Supp 5 column, was employed to analyze carboxylic acids and inorganic ions by Ionic chromatography (IC). The eluent was a $Na_2CO_3/NaHCO_3$ (3.2 mM/1.0 mM) buffer solution, while the anionic suppressor was a H_2SO_4 (100 mM) solution.

Table 1
Porous texture, average crystal size (D) and band gap (Eg) values.

	S_{BET} (m^2/g)	V_T (cm^3/g)	V_{MP} (cm^3/g)	D (nm)	Eg (eV)
Pt/NH_2-MIL-125	1243	0.68	0.55	31.9	2.48
Pd/NH_2-MIL-125	1248	0.70	0.55	31.0	2.50
Ag/NH_2-MIL-125	1083	0.57	0.48	31.8	2.70
NH_2-MIL-125	1109	0.59	0.47	32.3	2.56

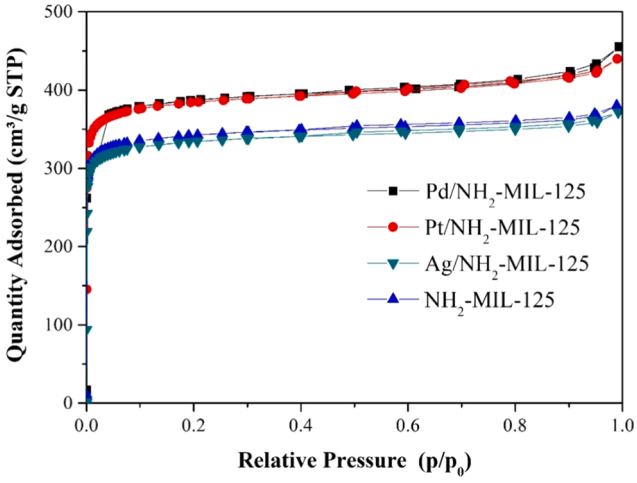

Fig. 2. N_2 adsorption–desorption isotherms at −196 °C.

3. Results and discussion

3.1. Characterization of the photocatalysts

Fig. 1 shows the XRD patterns of M/NH_2-MIL-125 compared with that of bare NH_2-MIL-125. All the materials synthesized described the characteristic pattern of NH_2-MIL-125 [22,28]. The most intense peaks appeared at 6.8, 9.5 and 11.6° values of 2θ, corresponding to the (0 1 1), (0 2 0) and (1 2 1) planes of NH_2-MIL-125, respectively [50]. The deposition of metal NPs did not modify significantly the XRD pattern of the bare NH_2-MIL-125, indicating that the crystalline structure of the MOF is maintained, without significant changes in the average crystal size (D) (see Table 1). The slight decrease observed is probably due to the thermal treatment following metal deposition. Similar results have been recently observed upon thermal stabilization of this same NH_2-MIL-125 MOF [51]. It is worth mentioning that no additional peaks are observed, not even those related to the impregnated metals, which can be explained by the low amount deposited (1 wt%) and more likely to the low size of the metallic nanoparticles, as will be confirmed later by the STEM images. The noble metal contents on M/NH_2-MIL-125 samples were quantified by ICP-MS analyses, resulting in 0.85, 0.92 and 0.98 wt % for Pt, Pd and Ag, respectively. These values are close to the theoretical 1 wt%, confirming the successful loading of the noble metals on NH_2-MIL-125 (Ti) MOF.

N_2 adsorption-desorption isotherms at −196 °C are depicted in Fig. 2 and Table 1 summarizes the resulting textural characteristics. All the isotherms follow the same pattern than that of the bare NH_2-MIL-125, indicative of essentially microporous solids with some small contribution of mesoporosity and high surface area values [53,54]. Therefore, as

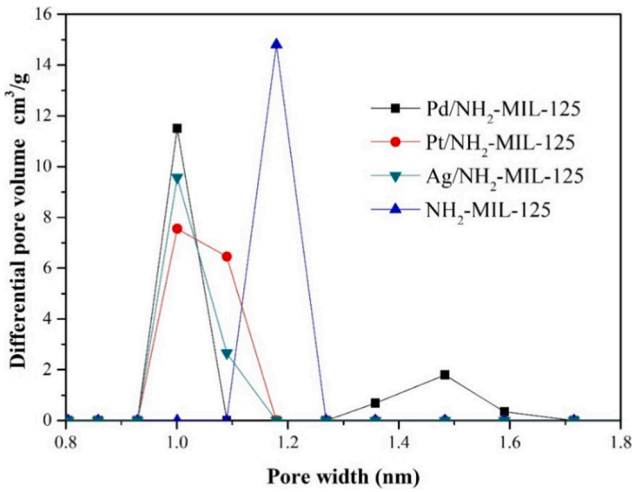

Fig. 3. DFT pore size distributions.

in the case of the crystalline structure, metal impregnation did not provoke significant changes on the porous texture of the original NH_2-MIL-125, except some increase of pore volume and surface area in the Pd and Pt/NH_2-MIL-125 samples but maintaining similar pattern. Pore size distribution (Fig. 3) shows some small displacement of the metal-impregnated samples towards narrower microporosity. These changes can be associated to the thermal treatment following metal deposition and are related to the removal of excess linker and/or remaining solvent molecules not completely removed by washing [51].

The UV–vis spectra are shown in Fig. 4A. All the solids show two absorption bands centred at 280 and 370 nm, due to Ti-oxo-clusters and linker, respectively [55,56]. M/NH_2-MIL-125 samples exhibit enhanced absorption in the visible range due to photons absorption of the metal NPs [23,50,57]. The absorption displayed by Ag/NH_2-MIL-125 is also associated with the surface plasmon resonance of Ag^0, an inherent property characterized by the redistribution of the charge density when the NPs are irradiated by light with a wavelength larger than their size [40,58]. The band gap values (E_g) (Table 1) were calculated using the Tauc plot method (Fig. 4B). All the materials yielded quite similar values (2.5–2.7 eV, see Table 1), indicating that, as expected, deposition of metal NPs does not modify the NH_2-MIL-125 band gap [23,24].

The surface composition of photocatalysts was analyzed by XPS. Figs. S2–S5 (supplementary information) show, respectively, the Ti 2p, C 1s, N 1s and O 1s deconvoluted spectra of the samples. The deconvolution of Ti 2p region profile gave two peaks at 464.5 and 458.8 eV, ascribed to the Ti^{4+} ions of the metal oxo-clusters in the MOF [28,59]. The C 1s spectra included four peaks located at 284.6, 285.3, 286.6 and 288.7 eV, which can be assessed to C═C/C—H, C—N, C═O/N—C═O and COO— moieties, respectively [28]. These peaks correspond to different bonds of the organic linker, 2-amino benzene dicarboxylic acid (NH_2-BDC) [28]. The O 1s deconvolution yielded three peaks, associated with the oxygen in Ti-oxo clusters (530.1 eV), the C═O bond (531.6 eV) of the linker and —OH groups (532.3 eV) [60]. Finally, deconvolution of the N 1s spectra gave three deconvoluted peaks at 399.3, 400.4 and 402.9 eV, derived from C—N/N—H, N—C═O and $—N^{+-}$, respectively [59]. These peaks are related to the positively charged nitrogen atoms and the N element of the amine functionality spreading or protruding into the empty space of the MOF [28,54]. Table 2 collects the surface elemental composition of all the materials from XPS spectra. No significant changes in Ti, O, N and C can be observed respect to the original NH_2-MIL-125. Comparison of the XPS surface values of each metal with the corresponding nominal bulk content (1%) suggests more likely egg-shell distribution for Ag and egg-yolk for Pd while Pt seems more evenly distributed.

Fig. 5 shows the deconvoluted spectra of Ag 3d, Pd 3d and Pt 4f of M/NH_2-MIL-125 samples and Table 3 collects the metal oxidation state determined from those spectra. The Pd 3d region of Pd/NH_2-MIL-125 shows two peaks at 335.0 and 340.3 eV associated to Pd^0. Meanwhile,

Table 2
XPS surface elemental composition.

Surface elemental composition (%)							
Sample	Ti	N	O	C	Pt	Pd	Ag
Pt/NH_2-MIL-125	38.45	4.28	33.03	23.41	0.83		
Pd/NH_2-MIL-125	39.02	4.64	33.09	22.99		0.26	
Ag/NH_2-MIL-125	37.29	5.08	32.83	22.58			2.23
NH_2-MIL-125	36.97	4.89	33.38	24.75			

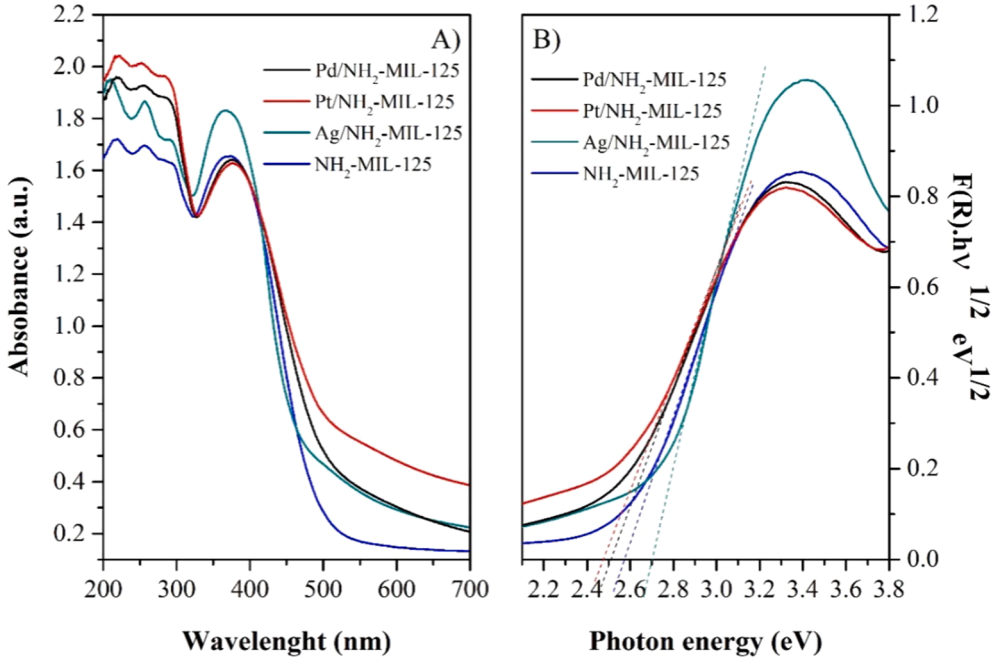

Fig. 4. (A) UV–Vis spectra and (B) Tauc plots.

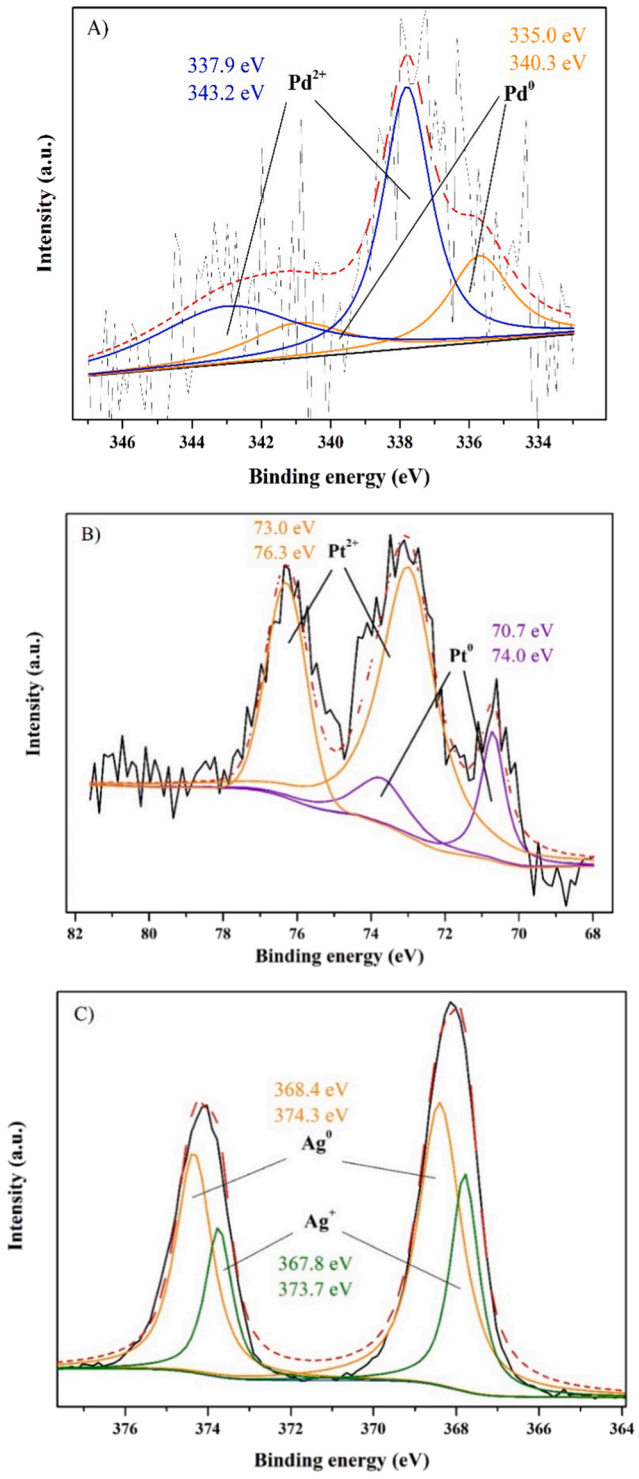

Fig. 5. (A) Pd 3d; (B) Pt 4f; (C) Ag 3d deconvoluted XPS spectra of Pd/NH_2-MIL-125, Pt/NH_2-MIL-125 and Ag/NH_2-MIL-125, respectively.

Table 3
Surface metal composition (estimated from XPS spectra) of M/NH_2-MIL-125.

Ag/NH_2-MIL-125			Pd/NH_2-MIL-125			Pt/NH_2-MIL-125		
Ag^+ (%)	Ag^0 (%)	Ag^+/Ag^0	Pd^{2+} (%)	Pd^0 (%)	Pd^{2+}/Pd^0	Pt^{2+} (%)	Pt^0 (%)	Pt^{2+}/Pt^0
34	66	0.50	65	35	1.83	79	21	3.81

two other peaks at 337.9 and 343.2 eV are ascribed to Pd^{2+}. Similar results were obtained when analyzing the Pt 4f region of Pt/NH_2-MIL-125, which displays two peaks at 70.7 and 74.0 eV, attributed to Pt^0, and two other peaks at 73.0 and 76.3 eV, assigned to Pt^{2+} [61]. The higher proportion of electrodeficient Pd and Pt on Pd/NH_2-MIL-125 and Pt/NH_2-MIL-125, respectively, can be due to the strong interaction of these metals with the MOF support and the relatively low reduction temperature (200 °C) used in order to preserve the MOF structure. Ag 3d region of Ag/NH_2-MIL-125 shows peaks at 368.4 and 374.3 eV confirming the presence of Ag^0, although other two peaks at 367.8 and 373.7 eV reveal also the presence of Ag^+ [40,62]. However, the Ag^+/Ag^0 ratio (Table 3) was quite low, verifying the successful photoreduction of the Ag precursor.

The presence of metallic NPs in the metal-loaded NH_2-MIL-125 was confirmed by STEM (Fig. 6). All synthesized materials show rectangular disk-like particles with an average size of 500 nm, characteristic of the NH_2-MIL-125 MOF [63,64]. The presence of metal NPs decorating the surface of the MOF appear as discrete spherical particles with average sizes of 3.8, 3.4 and 1.8 nm for Ag, Pt and Pd, respectively. In the case of Ag, the NPs show a bimodal distribution with most of the particles lower than 2 nm and other around 5 nm and higher in size (Fig. 6B). In contrast, both Pt and Pd show very uniform and evenly dispersed particles. Pd NPs are the smallest ones, difficult to observe in the lower magnification image (Fig. 6E). The metal NPs seem to be homogeneously distributed through the inner structure of the MOFs. It should be underlined that the location of those metal nanoparticle would have a very significant impact in the photoactivity of the resulting materials as previously show by Xiao et al. [65,66] when analysing the effect of the location of Pt nanoparticles on MOFs for the hydrogen production under visible light irradiation.

3.2. Photocatalytic tests

Adsorption of ACE onto the photocatalysts was checked prior to the reaction tests. Equilibrium was always reached in less than one hour and the adsorption capacity was in all the cases very low (Fig. S6). Those adsorption values were then used to adjust the pollutant concentration of the initial solution so that all the reaction tests started with ACE at 5 $mg{\cdot}L^{-1}$. Fig. 7 shows the evolution of ACE concentration upon irradiation time with the photocatalysts tested. In the absence of photocatalysis (photolysis) a negligible ACE degradation is obtained, which confirms the stability of this compound versus solar light. Metal nanoparticles clearly enhanced the rate of ACE removal respect to the observed with the bare titanium MOF. This positive effect of the metal NPs can be due to lower recombination of charges, as confirmed by the decreased intensity of PL spectra (shown in Fig. S7). It can be also ascribed to the enhanced light absorption in the visible range, as can be observed in UV–vis data (Fig. 4A). We have analysed by ICP-MS the presence of leached Pt in the aqueous solution after reaction using Pt/NH_2-MIL-125. The Pt concentration in the aqueous phase after reaction is very low (87 ppb), which corresponds to less than 3.5% of the initial Pt content of the photocatalyst and confirms the aqueous stability of the metal nanoparticles in the MOF.

The disappearance of ACE fits well to a pseudo-first-order rate equation (Fig. S8). The rate constant (k) values are included in Table 4, compared with those reported with other photocatalysts. Pt/NH_2-MIL-125 yielded the highest value, 2.4 times that of bare NH_2-MIL-125. That may be due to the combined effect of a better absorption of light in the visible range (Fig. 4A) and slower charges recombination rate (Fig. S7). The k value obtained with Pt/NH_2-MIL-125 is higher than that reported by a Zr-doped NH_2-MIL-125 (85%Ti/15%Zr) tested under the same reaction conditions [22], highlighting the light harvesting caused by the incorporation of Pt nanoparticles at surface of the MOF. Moreover, Pt/NH_2-MIL-125 also showed a higher k value than other photocatalysts designed by our research group, such as Ag/ZnO-TiO_2/clay heterostructure [40] or ZnO/sepiolite [67]. Nevertheless, this value is lower

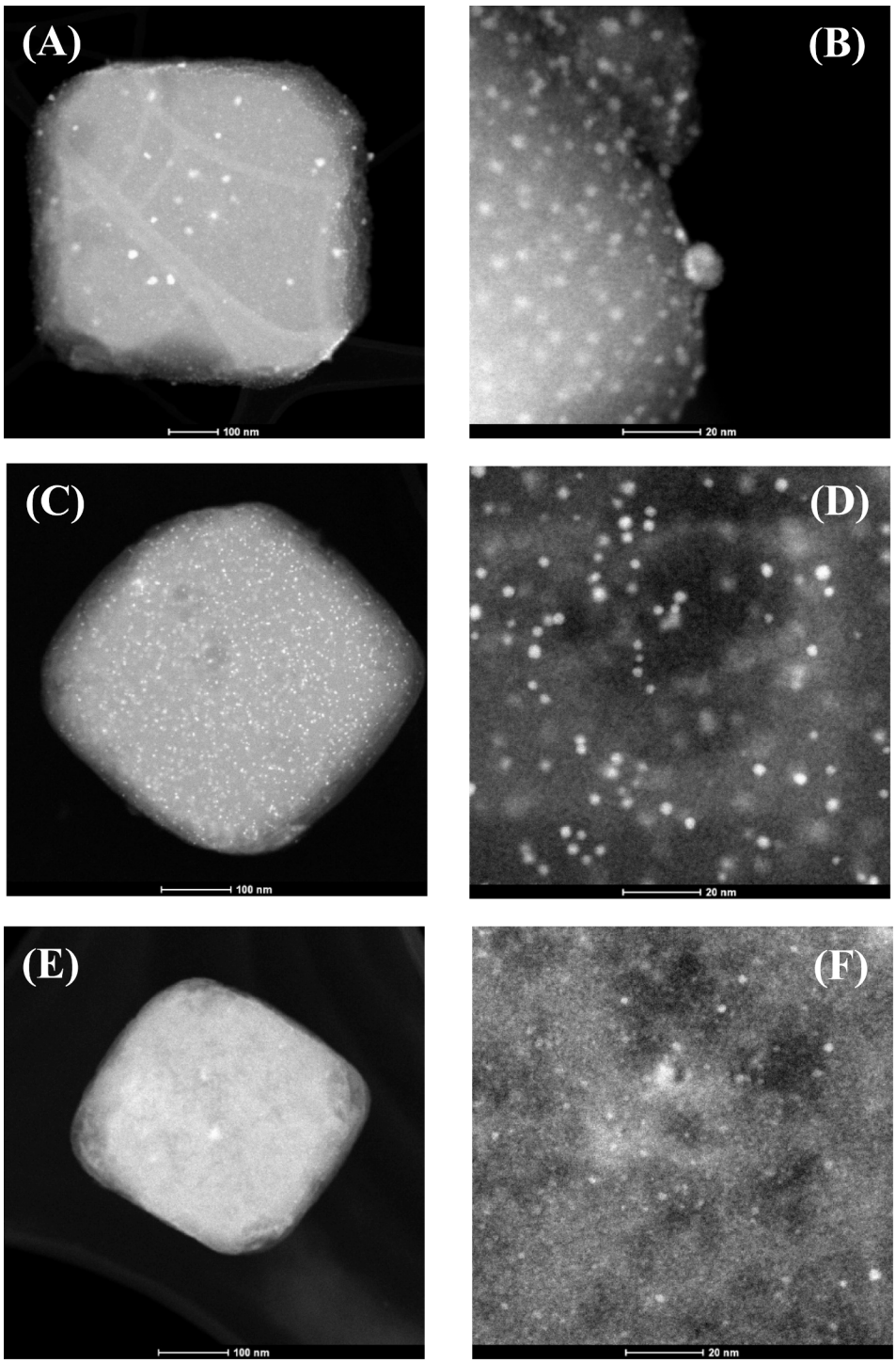

Fig. 6. STEM images of (A, B) Ag/NH_2-MIL-125, (C, D) Pt/NH_2-MIL-125 and (E, F) Pd/NH_2-MIL-125 (Bar lengths, left; 100 nm; right: 20 nm).

than that obtained with a heterojunction based on another MOF (Ag/AgCl@ZIF-8; 0.058 min^{-1}) [58], and also lower than the achieved by Pt/TiO_2 photocatalyst upon higher ACE and photocatalyst concentrations [68]. A higher rate constant was also reported by our group with C-modified TiO_2 under the same reaction conditions, related with the presence of anatase phase [69].

Several scavengers were used to learn on the main reactive species involved in the photocatalytic process. Fig. 8 A and B represent the ACE evolution upon irradiation time and the values of the pseudo-first order rate constant of ACE disappearance (k) with Pt/NH_2-MIL-125 in presence of different scavengers, respectively. KI (e^- scavenger) had no significant effect in the photocatalytic performance, so it can be said that the electrons do not participate actively in the degradation process. Meanwhile, the slight decrease of k with IPA ($^{\bullet}OH$ scavenger) indicate that hydroxyl radicals play a minor role in the ACE photodegradation with the catalysts tested. The breakdown rate was dramatically hindered in the presence of benzoquinone ($O_2^{\bullet-}$ scavenger), hence, the main reactive specie involved in ACE removal seems to be $O_2^{\bullet-}$. Besides this, the addition of $AgNO_3$ had an important effect, accelerating the disappearance of ACE. This effect can be attributed to the presence of Ag^+, which can absorb visible light giving rise to the formation of electrons and holes. These electrons can be transferred to the conduction band of

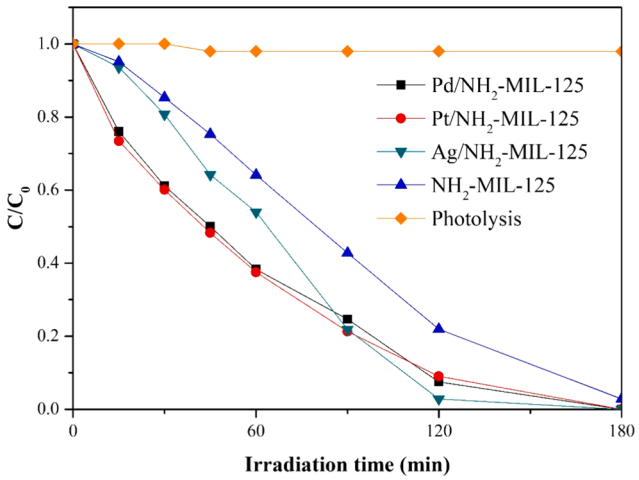

Fig. 7. Evolution of the ACE concentration under solar irradiation with the photocatalysts tested. ($[ACE]_o$ = 5 mg·L^{-1}; Photocatalyst load = 250 mg·L^{-1}; Illuminance = 107.14 klx).

Table 4
Values of the first order rate constant of ACE disappearance.

Catalyst	k (min^{-1})	Reference
Pt/NH_2-MIL-125	0.0165	This work
Pd/NH_2-MIL-125	0.0159	This work
Ag/NH_2-MIL-125	0.0096	This work
NH_2-MIL-125	0.0067	This work
NH_2-MIL-125 (85%Ti/15%Zr)	0.0121	[22]
ZnO/sepiolite	0.0032	[67]
Ag/ZnO-TiO_2/clay heterostructure	0.0095	[40]
Ag/AgCl@ZIF-8	0.0580	[58]
Pt/TiO_2	0.0260	[68]
C-modified TiO_2	0.0670	[69]

MOF, yielding more superoxide radicals [70]. The major role of superoxide radicals was also reported by Gómez-Aviles et al. [22] for the degradation of the same pharmaceutical (ACE) with Zr-doped NH_2-MIL-125 photocatalysts.

The water matrix can affect to the performance of photocatalytic degradation [75]. This potential effect was studied by mixing the starting ACE solution with chloride, nitrate, sulfate and carbonate ions, commonly present in water (Fig. 9). According to previous studies [71,72], chloride, nitrate and sulphate ions can react with hydroxyl radicals. Since these radicals do not significantly affect the reaction rate in the scavenger tests, the ACE photodegradation is not significantly affected by the presence of SO_4^- ions. Conversely, the presence of HCO_3^- caused a detrimental effect on the reaction. According to Liu et al [73], HCO_3^- ions interact with superoxide radicals, decreasing the $O_2^{\bullet-}$ concentration. Then, the observed decrease in the ACE degradation in the presence of HCO_3^- ions can be justified by the scavenging of superoxide radicals. A mixture of Cl^-, NO_3^-, SO_4^- and HCO_3^- ions was also tested under the same operating conditions and additional damage was observed, suggesting some synergistic negative effects.

The reusability of Pt/NH_2-MIL-125 catalyst was evaluated upon three successive cycles. ACE conversion decreased from the first to the

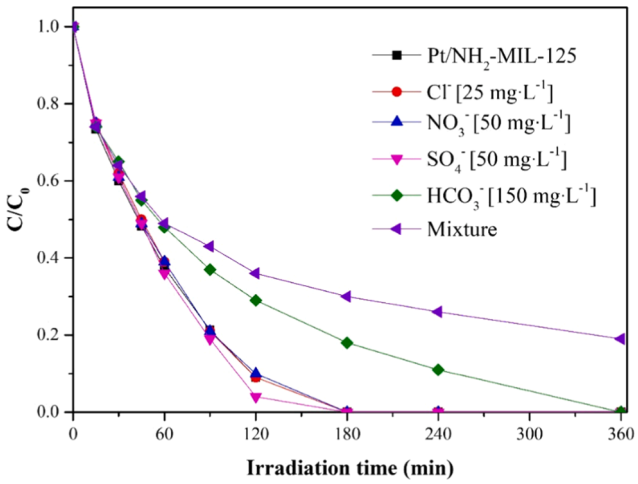

Fig. 9. Effect of some common inorganic ions on the photocatalytic degradation of ACE with Pt/NH_2-MIL-125 under solar irradiation (Operating conditions as in Fig. 7).

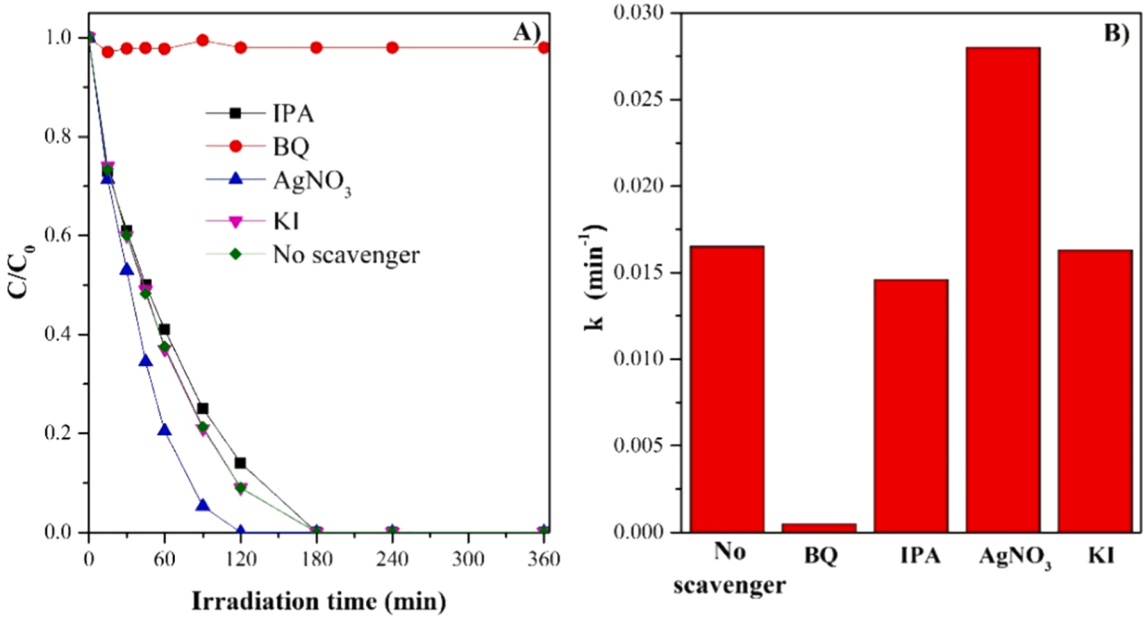

Fig. 8. (A) ACE evolution upon irradiation time and (B) values of the pseudo-first order rate constant of ACE disappearance (k) with Pt/NH_2-MIL-125 in presence of different scavengers.

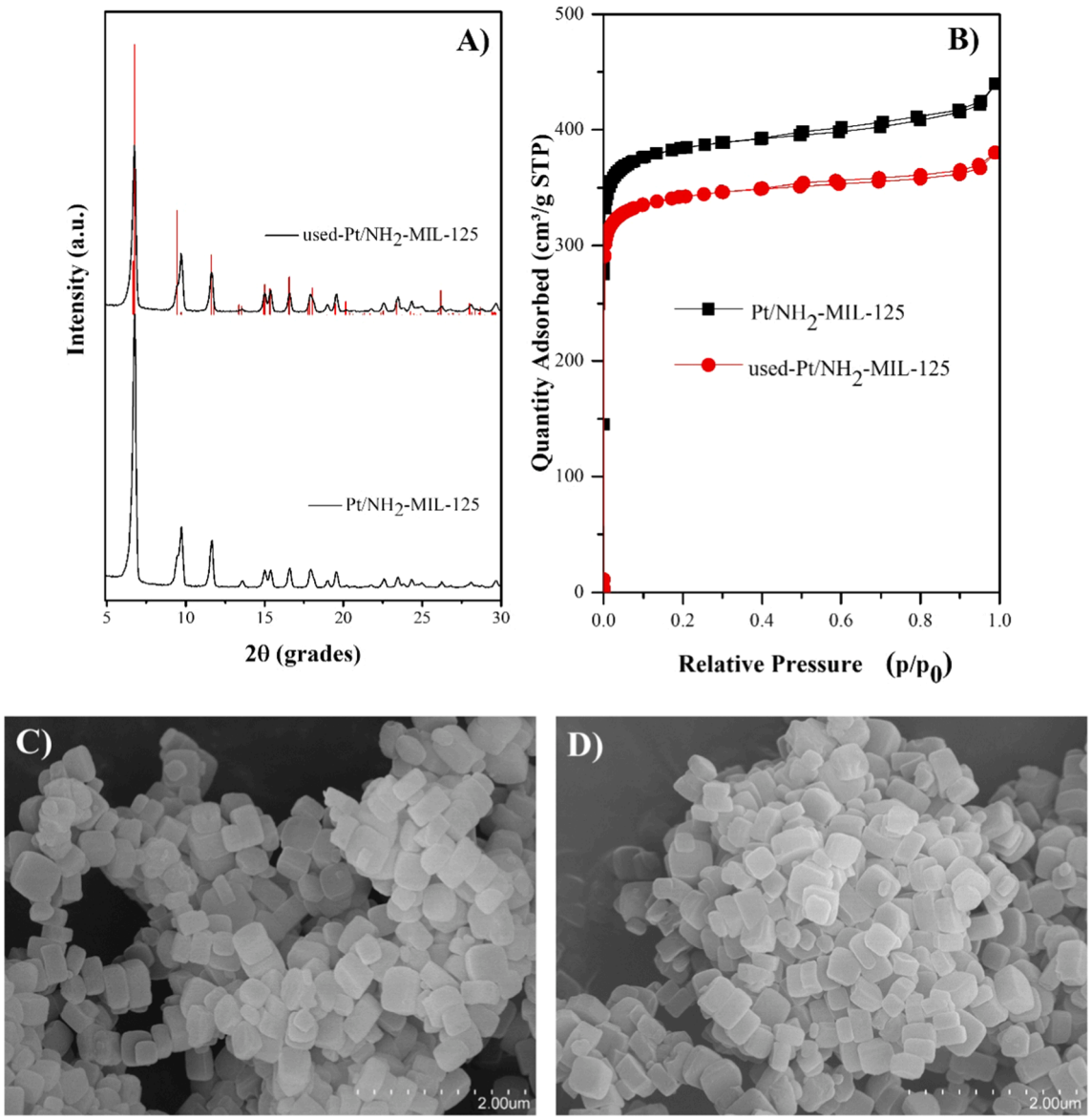

Fig. 10. Changes in the XRD pattern (A), nitrogen adsorption–desorption isotherms (B), and SEM images of Pt/NH_2-MIL-125 before (C) and after three successive cycles (D).

second cycle by about 8% and a further less than 5% decrease was observed in the third one. Similar behavior was reported for Zr-doped NH_2-MIL-125 photocatalyst [22] under the same reaction conditions. The photocatalytic activity decreased after the first cycle but remained almost unchanged from the second to the third runs, with conversion values above 90%. After the cycles, the photocatalyst was recovered and characterized by XRD, nitrogen adsorption–desorption and SEM micrographs (Fig. 10). Pt/NH_2-MIL-125 maintained its structure and porous texture, thus demonstrating its relatively high stability during the photocatalytic reaction. A small decrease (≈10%) of BET surface area was observed, probably due to some pore blockage caused by the adsorption of ACE and/or degradation by-products, probably responsible of the minor activity. No significant morphological changes were observed comparing the SEM images before (Fig. 10C) and after reaction (Fig. 10D). The particles maintained their rectangular disk-like shape with an average size of 500 nm, in agreement with TEM images (Fig. 6).

The reaction intermediates were identified by LC/ESI.MS and IC. The accurate mass (m/z) of the detected by-products is summarized in Table S1. The low mass error (<±1 mDa) and the value of ring and double bonds (RDB) corroborated the chemical species. RDB is related to numbers of rings and double bonds in the molecules. Based on the detected compounds, a proposed degradation pathway is depicted in Fig. 11. One of the reaction pathways consists on the coupling of ACE molecules. Thus, two ACE molecules can form ACE-2 (m/z 301.1181), previously reported by Chen et al. [84]. Then, the direct aromatic ring hydroxylation of ACE-2 yield ACE-3 compound (non-detected, but previously observed in the literature [75]), which can be further hydroxylated in ACE-4 (m/z 349.1030). On the other hand, the ring opening of ACE molecules can give rise to the formation of ACE-1 or butylamine (m/z 74.0958), and maleic and malonic acids. These acids were also detected in previous studies [76–78]. Further oxidation of these intermediates produces formic and acetic acids. Finally, the mineralization of these short-chain acids leads the formation of CO_2, NO_3^- and H_2O. Only nitrate is detected as mineralization nitrogen product.

4. Conclusions

Noble metal (Ag, Pd and Pt) nanoparticles were successfully deposited on NH_2-MIL-125 by wet impregnation followed by a reduction treatment. The characteristic structure of the MOF was maintained in all

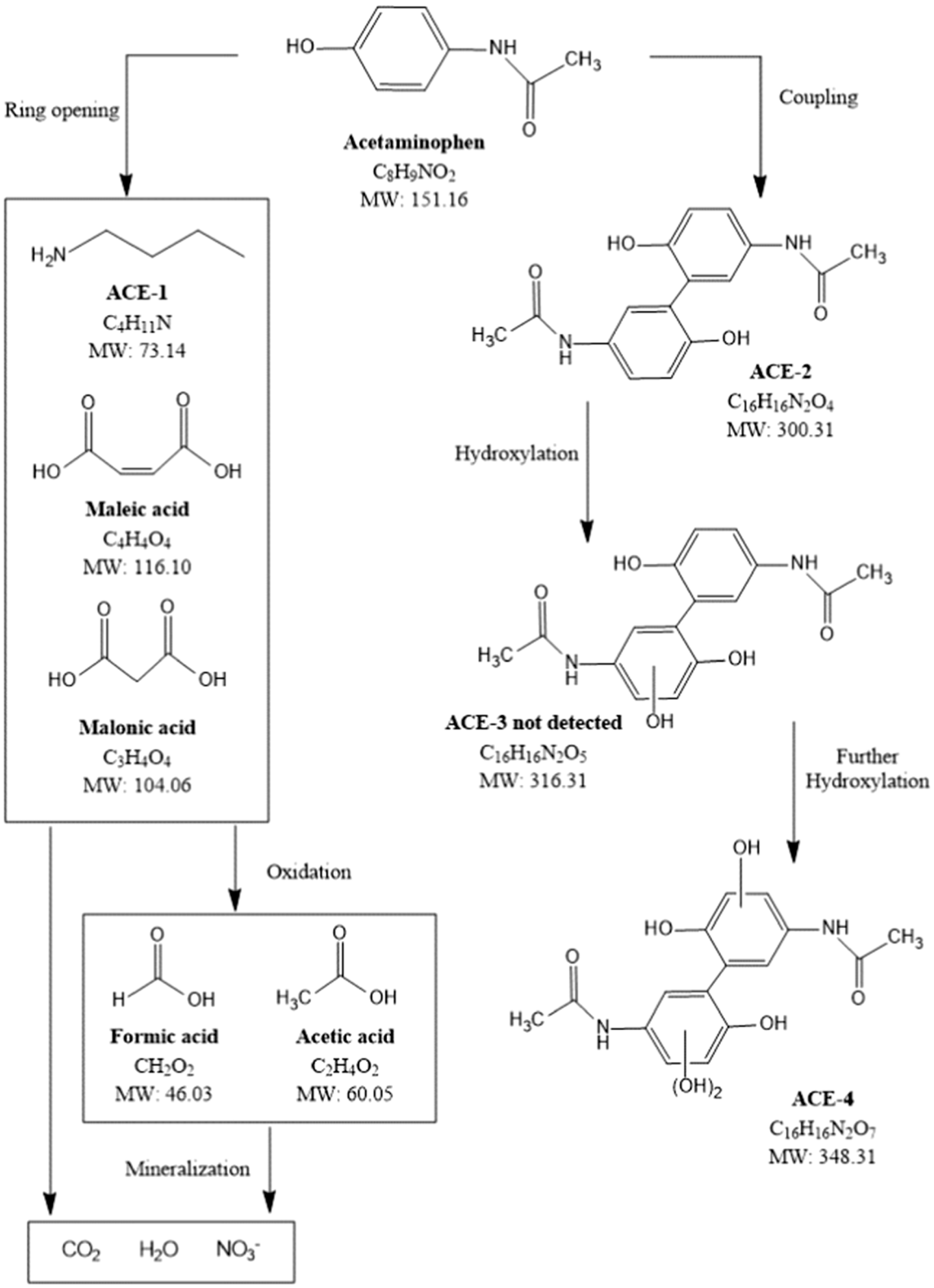

Fig. 11. Proposed reaction pathway for ACE photocatalytic degradation with Pt/NH_2-MIL-125.

M/NH_2-MIL-125 as well as the microporous texture with high surface area. Metal nanoparticles appeared decorating the surface of the MOF, with average sizes from 1.8 to 3.5 nm depending of the metal. Those nanoparticles were a mixture of M^{2+}/M^0 species responsible of light absorption in the visible region. The Pt/NH_2-MIL-125 photocatalyst yielded the best results in the degradation of the target pollutant (ACE), due to enhanced visible light absorption and slower recombination of the photogenerated charges. $O_2^{\bullet-}$ radicals governed the ACE photodegradation process. The photocatalytic performance of Pt/NH_2-MIL-125 was not significantly affected by the presence of Cl^-, NO_3^- and SO_4^- ions, while HCO_3^- caused a detrimental effect due to $O_2^{\bullet-}$ trapping. The stability and reusability of Pt/NH_2-MIL-125 was tested upon three

successive cycles, where its original crystalline structure and porous texture were maintained. Some small decrease of activity was observed as inferred from the reduction of ACE conversion (somewhat above 10% after the three cycles).

CRediT authorship contribution statement

V. Muelas-Ramos: Methodology, Writing - original draft, Writing - review & editing. **C. Belver:** Conceptualization, Writing - review & editing, Supervision, Funding acquisition. **J.J. Rodríguez:** Conceptualization, Writing - review & editing, Supervision, Funding acquisition. **J. Bedia:** Conceptualization, Writing - review & editing, Supervision, Funding acquisition.

Declaration of Competing Interest

The authors declare that they have no known competing financial interests or personal relationships that could have appeared to influence the work reported in this paper.

Acknowledgements

This research was funded by the State Research Agency (PID2019-106186RB-I00/AEI/10.13039/501100011033). V. Muelas-Ramos thanks to MCIU for BES-2017-082613 grant. Authors thank the Research Support Services of XPS data from University of Málaga (Spain) and STEM images from Instituto de Nanociencia de Aragón (University of Zaragoza, Spain).

Appendix A. Supplementary material

Supplementary data to this article can be found online at https://doi.org/10.1016/j.seppur.2021.118896.

References

[1] J.L. Acero, F.J. Benitez, F.J. Real, F. Teva, Removal of emerging contaminants from secondary effluents by micellar-enhanced ultrafiltration, Sep. Purif. Technol. 181 (2017) 123–131, https://doi.org/10.1016/j.seppur.2017.03.021.

[2] Y. Yang, Y.S. Ok, K.H. Kim, E.E. Kwon, Y.F. Tsang, Occurrences and removal of pharmaceuticals and personal care products (PPCPs) in drinking water and water/sewage treatment plants: A review, Sci. Total Environ. 596–597 (2017) 303–320, https://doi.org/10.1016/j.scitotenv.2017.04.102.

[3] L. Rizzo, S. Malato, D. Antakyali, V.G. Beretsou, M.B. Đolić, W. Gernjak, E. Heath, I. Ivancev-Tumbas, P. Karaolia, A.R. Lado Ribeiro, G. Mascolo, C.S. McArdell, H. Schaar, A.M.T. Silva, D. Fatta-Kassinos, Consolidated vs new advanced treatment methods for the removal of contaminants of emerging concern from urban wastewater, Sci. Total Environ. 655 (2019) 986–1008, https://doi.org/10.1016/j.scitotenv.2018.11.265.

[4] C. Byrne, G. Subramanian, S.C. Pillai, Recent advances in photocatalysis for environmental applications, J. Environ. Chem. Eng. 6 (2018) 3531–3555, https://doi.org/10.1016/j.jece.2017.07.080.

[5] A. Fujishima, K. Honda, Electrochemical Photolysis of Water at a Semiconductor Electrode, Nature 238 (1972) 37–38, https://doi.org/10.1038/238037a0.

[6] R. Daghrir, P. Drogui, D. Robert, Modified TiO_2 for environmental photocatalytic applications: A review, Ind. Eng. Chem. Res. 52 (2013) 3581–3599, https://doi.org/10.1021/ie303468t.

[7] Z. Shayegan, C.S. Lee, F. Haghighat, TiO_2 photocatalyst for removal of volatile organic compounds in gas phase – A review, Chem. Eng. J. 334 (2018) 2408–2439, https://doi.org/10.1016/j.cej.2017.09.153.

[8] Y. Cui, L. Chao Nengzi, J. Gou, Y. Huang, B. Li, X. Cheng, Fabrication of dual Z-scheme MIL-53(Fe)/A-Bi_2O_3/g-C_3N_4 ternary composite with enhanced visible light photocatalytic performance, Sep. Purif. Technol. 232 (2020), https://doi.org/10.1016/j.seppur.2019.115959.

[9] Y. Lin, C. Kong, Q. Zhang, L. Chen, Metal-Organic Frameworks for Carbon Dioxide Capture and Methane Storage, Adv. Energy Mater. 7 (2017) 1601296, https://doi.org/10.1002/aenm.201601296.

[10] Y. He, W. Zhou, G. Qian, B. Chen, Methane storage in metal–organic frameworks, Chem. Soc. Rev. 43 (2014) 5657–5678, https://doi.org/10.1039/C4CS00032C.

[11] K. Meyer, M. Ranocchiari, J.A. van Bokhoven, Metal organic frameworks for photocatalytic water splitting, Energy Environ. Sci. 8 (2015) 1923–1937, https://doi.org/10.1039/C5EE00161G.

[12] H. Song, Z. Sun, Y. Xu, Y. Han, J. Xu, J. Wu, T. Sun, H. Meng, X. Zhang, Fabrication of NH_2-MIL-125(Ti) incorporated TiO_2 nanotube arrays composite anodes for highly efficient PEC water splitting, Sep. Purif. Technol. 228 (2019), 115764, https://doi.org/10.1016/j.seppur.2019.115764.

[13] R.J. Kuppler, D.J. Timmons, Q.-R. Fang, J.-R. Li, T.A. Makal, M.D. Young, D. Yuan, D. Zhao, W. Zhuang, H.-C. Zhou, Potential applications of metal-organic frameworks, Coord. Chem. Rev. 253 (2009) 3042–3066, https://doi.org/10.1016/j.ccr.2009.05.019.

[14] H. Li, K. Wang, Y. Sun, C.T. Lollar, J. Li, H.-C. Zhou, Recent advances in gas storage and separation using metal–organic frameworks, Mater. Today. 21 (2018) 108–121, https://doi.org/10.1016/J.MATTOD.2017.07.006.

[15] J.B. DeCoste, G.W. Peterson, Metal-Organic Frameworks for Air Purification of Toxic Chemicals, Chem. Rev. 114 (2014) 5695–5727, https://doi.org/10.1021/cr4006473.

[16] M.L. Hu, V. Safarifard, E. Doustkhah, S. Rostamnia, A. Morsali, N. Nouruzi, S. Beheshti, K. Akhbari, Taking organic reactions over metal-organic frameworks as heterogeneous catalysis, Microporous Mesoporous Mater. 256 (2018) 111–127, https://doi.org/10.1016/j.micromeso.2017.07.057.

[17] S.W. Lv, J.M. Liu, N. Zhao, C.Y. Li, F.E. Yang, Z.H. Wang, S. Wang, MOF-derived $CoFe_2O_4/Fe_2O_3$ embedded in g-C_3N_4 as high-efficient Z-scheme photocatalysts for enhanced degradation of emerging organic pollutants in the presence of persulfate, Sep. Purif. Technol. 253 (2020), 117413, https://doi.org/10.1016/j.seppur.2020.117413.

[18] J. Bedia, V. Muelas-Ramos, M. Peñas-Garzón, A. Gómez-Avilés, J. Rodríguez, C. Belver, A Review on the Synthesis and Characterization of Metal Organic Frameworks for Photocatalytic Water Purification, Catalysts 9 (2019) 52, https://doi.org/10.3390/catal9010052.

[19] Z. Shao, D. Zhang, H. Li, C. Su, X. Pu, Y. Geng, Fabrication of MIL-88A/g-C_3N_4 direct Z-scheme heterojunction with enhanced visible-light photocatalytic activity, Sep. Purif. Technol. 220 (2019) 16–24, https://doi.org/10.1016/j.seppur.2019.03.040.

[20] M. Dan-Hardi, C. Serre, T. Frot, L. Rozes, G. Maurin, C. Sanchez, G. Férey, A New Photoactive Crystalline Highly Porous Titanium(IV) Dicarboxylate, J. Am. Chem. Soc. 131 (2009) 10857–10859, https://doi.org/10.1021/ja903726m.

[21] C.H. Hendon, D. Tiana, M. Fontecave, C.C. Sanchez, L. D'arras, C. Sassoye, L. Rozes, C. Mellot-Draznieks, A. Walsh, L. D'Arras, C. Sassoye, L. Rozes, C. Mellot-Draznieks, A. Walsh, Engineering the optical response of the titanium-MIL-125 metal-organic framework through ligand functionalization, J. Am. Chem. Soc. 135 (2013) 10942–10945, https://doi.org/10.1021/ja405350u.

[22] A. Gómez-Avilés, M. Peñas-Garzón, J. Bedia, D.D. Dionysiou, J.J. Rodríguez, C. Belver, Mixed Ti-Zr metal-organic-frameworks for the photodegradation of acetaminophen under solar irradiation, Appl. Catal. B Environ. 253 (2019) 253–262, https://doi.org/10.1016/j.apcatb.2019.04.040.

[23] R.M. Abdelhameed, M.M.Q. Simões, A.M.S. Silva, J. Rocha, Enhanced Photocatalytic Activity of MIL-125 by Post-Synthetic Modification with Cr^{III} and Ag Nanoparticles, Chem. – A Eur. J. 21 (2015) 11072–11081, https://doi.org/10.1002/chem.201500808.

[24] Y. Fu, H. Yang, R. Du, G. Tu, C. Xu, F. Zhang, M. Fan, W. Zhu, Enhanced photocatalytic CO_2 reduction over Co-doped NH_2 -MIL-125(Ti) under visible light, RSC Adv. 7 (2017) 42819–42825, https://doi.org/10.1039/C7RA06324E.

[25] Q. Hu, J. Di, B. Wang, M. Ji, Y. Chen, J. Xia, H. Li, Y. Zhao, In-situ preparation of NH 2 -MIL-125(Ti)/BiOCl composite with accelerating charge carriers for boosting visible light photocatalytic activity, Appl. Surf. Sci. 466 (2019) 525–534, https://doi.org/10.1016/j.apsusc.2018.10.020.

[26] A. Rahmani, H.B.M. Emrooz, S. Abedi, A. Morsali, Synthesis and characterization of CdS/MIL-125 (Ti) as a photocatalyst for water splitting, Mater. Sci. Semicond. Process. 80 (2018) 44–51, https://doi.org/10.1016/j.mssp.2018.02.013.

[27] H. Wang, X. Yuan, Y. Wu, G. Zeng, X. Chen, L. Leng, H. Li, Synthesis and applications of novel graphitic carbon nitride/metal-organic frameworks mesoporous photocatalyst for dyes removal, Appl. Catal. B Environ. 174–175 (2015) 445–454, https://doi.org/10.1016/j.apcatb.2015.03.037.

[28] S.-R. Zhu, P.-F. Liu, M.-K. Wu, W.-N. Zhao, G.-C. Li, K. Tao, F.-Y. Yi, L. Han, Enhanced photocatalytic performance of BiOBr/NH_2-MIL-125(Ti) composite for dye degradation under visible light, Dalt. Trans. 45 (2016) 17521–17529, https://doi.org/10.1039/C6DT02912D.

[29] H. Wang, X. Yuan, Y. Wu, G. Zeng, H. Dong, X. Chen, L. Leng, Z. Wu, L. Peng, In situ synthesis of In_2S_3@MIL-125(Ti) core–shell microparticle for the removal of tetracycline from wastewater by integrated adsorption and visible-light-driven photocatalysis, Appl. Catal. B Environ. 186 (2016) 19–29, https://doi.org/10.1016/J.APCATB.2015.12.041.

[30] X. Li, Y. Pi, Q. Hou, H. Yu, Z. Li, Y. Li, J. Xiao, Amorphous TiO_2@NH_2-MIL-125(Ti) homologous MOF-encapsulated heterostructures with enhanced photocatalytic activity, Chem. Commun. 54 (2018) 1917–1920, https://doi.org/10.1039/c7cc09072b.

[31] W. Jiang, Z. Li, C. Liu, D. Wang, G. Yan, B. Liu, G. Che, Enhanced visible-light-induced photocatalytic degradation of tetracycline using BiOI/MIL-125(Ti) composite photocatalyst, J. Alloys Compd. 854 (2021), 157166, https://doi.org/10.1016/j.jallcom.2020.157166.

[32] H. Wang, P.H. Cui, J.X. Shi, J.Y. Tan, J.Y. Zhang, N. Zhang, C. Zhang, Controllable self-assembly of CdS@NH2-MIL-125(Ti) heterostructure with enhanced photodegradation efficiency for organic pollutants through synergistic effect, Mater. Sci. Semicond. Process. 97 (2019) 91–100, https://doi.org/10.1016/j.mssp.2019.03.016.

[33] S. Yin, Y. Chen, C. Gao, Q. Hu, M. Li, Y. Ding, J. Di, J. Xia, H. Li, In-situ preparation of MIL-125(Ti)/Bi_2WO_6 photocatalyst with accelerating charge carriers for the photodegradation of tetracycline hydrochloride, J. Photochem. Photobiol. A Chem. 387 (2020), 112149, https://doi.org/10.1016/j.jphotochem.2019.112149.

[34] M. Salimi, A. Esrafili, A. Jonidi Jafari, M. Gholami, H.R. Sobhi, M. Nourbakhsh, B. Akbari-Adergani, Photocatalytic degradation of cefixime with MIL-125(Ti)-mixed linker decorated by g-C3N4 under solar driven light irradiation, Colloids Surfaces A Physicochem. Eng. Asp. 582 (2019), 123874, https://doi.org/10.1016/j.colsurfa.2019.123874.

[35] R.M. Abdelhameed, M. El-Shahat, H.E. Emam, Employable metal (Ag & Pd)@MIL-125-NH_2@cellulose acetate film for visible-light driven photocatalysis for reduction of nitro-aromatics, Carbohydr. Polym. 247 (2020), 116695, https://doi.org/10.1016/j.carbpol.2020.116695.

[36] D. Sun, W. Liu, Y. Fu, Z. Fang, F. Sun, X. Fu, Y. Zhang, Z. Li, Noble Metals Can Have Different Effects on Photocatalysis Over Metal-Organic Frameworks (MOFs): A Case Study on M/NH_2-MIL-125(Ti) (M=Pt and Au), Chem. – A Eur. J. 20 (2014) 4780–4788, https://doi.org/10.1002/chem.201304067.

[37] C. Hou, Q. Xu, Y. Wang, X. Hu, Synthesis of Pt@NH_2-MIL-125(Ti) as a photocathode material for photoelectrochemical hydrogen production, RSC Adv. 3 (2013) 19820, https://doi.org/10.1039/c3ra43188f.

[38] J. Qiu, L. Yang, M. Li, J. Yao, Metal nanoparticles decorated MIL-125-NH_2 and MIL-125 for efficient photocatalysis, Mater. Res. Bull. 112 (2019) 297–306, https://doi.org/10.1016/J.MATERRESBULL.2018.12.038.

[39] M. Martis, W. Meicheng, K. Mori, H. Yamashita, Fabrication of metal nanoparticles in metal organic framework NH2-MIL-125 by UV photo-assisted methods for optimized catalytic properties, Catal. Today. 235 (2014) 98–102, https://doi.org/10.1016/J.CATTOD.2014.02.046.

[40] C. Belver, M. Hinojosa, J. Bedia, M. Tobajas, M. Alvarez, V. Rodríguez-González, J. Rodriguez, Ag-Coated Heterostructures of ZnO-TiO_2/Delaminated Montmorillonite as Solar Photocatalysts, Materials (Basel). 10 (2017) 960, https://doi.org/10.3390/ma10080960.

[41] K.S. Walton, R.Q. Snurr, Applicability of the BET method for determining surface areas of microporous metal-organic frameworks, J. Am. Chem. Soc. 129 (2007) 8552–8556, https://doi.org/10.1021/ja071174k.

[42] A.J. Howarth, A.W. Peters, N.A. Vermeulen, T.C. Wang, J.T. Hupp, O.K. Farha, Best practices for the synthesis, activation, and characterization of metal−organic frameworks, Chem. Mater. 29 (2017) 26–39, https://doi.org/10.1021/acs.chemmater.6b02626.

[43] J. Tauc, Absorption edge and internal electric fields in amorphous semiconductors, Mater. Res. Bull. 5 (1970) 721–729, https://doi.org/10.1016/0025-5408(70)90112-1.

[44] P.V. Hlophe, L.C. Mahlalela, L.N. Dlamini, A composite of platelet-like orientated $BiVO_4$ fused with MIL-125(Ti): Synthesis and characterization, Sci. Rep. 9 (2019) 1–12, https://doi.org/10.1038/s41598-019-46498-w.

[45] M. Yin, Z. Li, J. Kou, Z. Zou, Mechanism Investigation of Visible Light-Induced Degradation in a Heterogeneous TiO_2/Eosin Y/Rhodamine B System, Environ. Sci. Technol. 43 (2009) 8361–8366, https://doi.org/10.1021/es902011h.

[46] L. Ye, J. Liu, Z. Jiang, T. Peng, L. Zan, Facets coupling of BiOBr-g-C_3N_4 composite photocatalyst for enhanced visible-light-driven photocatalytic activity, Appl. Catal. B Environ. 142–143 (2013) 1–7, https://doi.org/10.1016/J.APCATB.2013.04.058.

[47] M. Fakhrul Ridhwan Samsudin, L. Tau Siang, S. Sufian, R. Bashiri, N. Muti Mohamed, R. Mahirah Ramli, Exploring the role of electron-hole scavengers on optimizing the photocatalytic performance of BiVO4, in: Mater. Today Proc., Elsevier Ltd, 2018, pp. 21703–21709. doi: 10.1016/j.matpr.2018.07.022.

[48] Y. Wang, P. Zhang, Photocatalytic decomposition of perfluorooctanoic acid (PFOA) by TiO_2 in the presence of oxalic acid, J. Hazard. Mater. 192 (2011) 1869–1875, https://doi.org/10.1016/J.JHAZMAT.2011.07.026.

[49] A. Gómez-Avilés, M. Peñas-Garzón, J. Bedia, D.D. Dionysiou, J.J. Rodriguez, C. Belver, Mixed Ti-Zr metal-organic-frameworks for the photodegradation of acetaminophen under solar irradiation, Appl. Catal B Environ. 253 (2019) 253–262, https://doi.org/10.1016/J.APCATB.2019.04.040.

[50] F.B. Li, X.Z. Li, The enhancement of photodegradation efficiency using Pt-TiO_2 catalyst, Chemosphere 48 (2002) 1103–1111, https://doi.org/10.1016/S0045-6535(02)00201-1.

[51] A. Gómez-Avilés, V. Muelas-Ramos, J. Bedia, J.J. Rodriguez, C. Belver, Thermal Post-Treatments to Enhance the Water Stability of NH_2-MIL-125(Ti), Catalysts 10 (2020) 603, https://doi.org/10.3390/catal10060603.

[52] A.P. Smalley, D.G. Reid, J.C. Tan, G.O. Lloyd, Alternative synthetic methodology for amide formation in the post-synthetic modification of Ti-MIL125-NH_2, CrystEngComm 15 (2013) 9368, https://doi.org/10.1039/c3ce41332b.

[53] S.-N. Kim, J. Kim, H.-Y. Kim, H.-Y. Cho, W.-S. Ahn, Adsorption/catalytic properties of MIL-125 and NH_2-MIL-125, Catal. Today 204 (2013) 85–93, https://doi.org/10.1016/J.CATTOD.2012.08.014.

[54] H. Wang, X. Yuan, Y. Wu, G. Zeng, X. Chen, L. Leng, Z. Wu, L. Jiang, H. Li, Facile synthesis of amino-functionalized titanium metal-organic frameworks and their superior visible-light photocatalytic activity for Cr(VI) reduction, J. Hazard. Mater. 286 (2015) 187–194, https://doi.org/10.1016/j.jhazmat.2014.11.039.

[55] Y. Fu, L. Sun, H. Yang, L. Xu, F. Zhang, W. Zhu, Visible-light-induced aerobic photocatalytic oxidation of aromatic alcohols to aldehydes over Ni-doped NH_2-MIL-125(Ti), Appl. Catal. B Environ. 187 (2016) 212–217, https://doi.org/10.1016/J.APCATB.2016.01.038.

[56] Y. Fu, D. Sun, Y. Chen, R. Huang, Z. Ding, X. Fu, Z. Li, An Amine-Functionalized Titanium Metal-Organic Framework Photocatalyst with Visible-Light-Induced Activity for CO_2 Reduction, Angew. Chem. Int. Ed. 51 (2012) 3364–3367, https://doi.org/10.1002/anie.201108357.

[57] S.H. Hsieh, W.J. Chen, C.T. Wu, Pt-TiO_2/graphene photocatalysts for degradation of AO7 dye under visible light, Appl. Surf. Sci. 340 (2015) 9–17, https://doi.org/10.1016/j.apsusc.2015.02.184.

[58] G. Fan, X. Zheng, J. Luo, H. Peng, H. Lin, M. Bao, L. Hong, J. Zhou, Rapid synthesis of Ag/AgCl@ZIF-8 as a highly efficient photocatalyst for degradation of acetaminophen under visible light, Chem. Eng. J. 351 (2018) 782–790, https://doi.org/10.1016/J.CEJ.2018.06.119.

[59] M. Wang, L. Yang, J. Yuan, L. He, Y. Song, H. Zhang, Z. Zhang, S. Fang, Heterostructured Bi_2S_3@NH_2-MIL-125(Ti) nanocomposite as a bifunctional photocatalyst for Cr(vi) reduction and rhodamine B degradation under visible light, RSC Adv. 8 (2018) 12459–12470, https://doi.org/10.1039/c8ra00882e.

[60] H. Liu, J. Zhang, D. Ao, Construction of heterostructured $ZnIn_2S_4$@NH_2-MIL-125 (Ti) nanocomposites for visible-light-driven H_2 production, Appl. Catal. B Environ. 221 (2018) 433–442, https://doi.org/10.1016/J.APCATB.2017.09.043.

[61] J. Fan, K. Qi, L. Zhang, H. Zhang, S. Yu, X. Cui, Engineering Pt/Pd Interfacial Electronic Structures for Highly Efficient Hydrogen Evolution and Alcohol Oxidation, ACS Appl. Mater. Interfaces 9 (2017) 18008–18014, https://doi.org/10.1021/acsami.7b05290.

[62] C. Belver, C. Adán, S. García-Rodríguez, M. Fernández-García, Photocatalytic behavior of silver vanadates: Microemulsion synthesis and post-reaction characterization, Chem. Eng. J. 224 (2013) 24–31, https://doi.org/10.1016/j.cej.2012.11.102.

[63] R.M. Abdelhameed, D.M. Tobaldi, M. Karmaoui, Engineering highly effective and stable nanocomposite photocatalyst based on NH_2-MIL-125 encirclement with Ag_3PO_4 nanoparticles, J. Photochem. Photobiol. A Chem. 351 (2018) 50–58, https://doi.org/10.1016/J.JPHOTOCHEM.2017.10.011.

[64] J. Xu, J. Gao, C. Wang, Y. Yang, L. Wang, NH2-MIL-125(Ti)/graphitic carbon nitride heterostructure decorated with NiPd co-catalysts for efficient photocatalytic hydrogen production, Appl. Catal. B Environ. 219 (2017) 101–108, https://doi.org/10.1016/j.apcatb.2017.07.046.

[65] J.-D. Xiao, L. Han, J. Luo, S.-H. Yu, H.-L. Jiang, Integration of Plasmonic Effects and Schottky Junctions into Metal-Organic Framework Composites: Steering Charge Flow for Enhanced Visible-Light Photocatalysis, Angew. Chemie Int. Ed. 57 (2018) 1103–1107, https://doi.org/10.1002/anie.201711725.

[66] J. Xiao, Q. Shang, Y. Xiong, Q. Zhang, Y. Luo, S. Yu, H. Jiang, Boosting Photocatalytic Hydrogen Production of a Metal-Organic Framework Decorated with Platinum Nanoparticles: The Platinum Location Matters, Angew. Chem. 128 (2016) 9535–9539, https://doi.org/10.1002/ange.201603990.

[67] M. Akkari, P. Aranda, C. Belver, J. Bedia, A. Ben Haj Amara, E. Ruiz-Hitzky, ZnO/sepiolite heterostructured materials for solar photocatalytic degradation of pharmaceuticals in wastewater, Appl. Clay Sci. 156 (2018) 104–109. doi: 10.1016/j.clay.2018.01.021.

[68] O. Nasr, O. Mohamed, A.S. Al-Shirbini, A.M. Abdel-Wahab, Photocatalytic degradation of acetaminophen over Ag, Au and Pt loaded TiO_2 using solar light, J. Photochem. Photobiol. A Chem. 374 (2019) 185–193, https://doi.org/10.1016/j.jphotochem.2019.01.032.

[69] A. Gómez-Avilés, M. Peñas-Garzón, J. Bedia, J.J. Rodriguez, C. Belver, C-modified TiO_2 using lignin as carbon precursor for the solar photocatalytic degradation of acetaminophen, Chem. Eng. J. 358 (2019) 1574–1582, https://doi.org/10.1016/j.cej.2018.10.154.

[70] L. Ye, J. Liu, C. Gong, L. Tian, T. Peng, L. Zan, Two different roles of metallic Ag on Ag/AgX/BiOX (X = Cl, Br) visible light photocatalysts: Surface plasmon resonance and Z-Scheme bridge, ACS Catal. 2 (2012) 1677–1683, https://doi.org/10.1021/cs300213m.

[71] E. Kudlek, M. Dudziak, J. Bohdziewicz, Influence of Inorganic Ions and Organic Substances on the Degradation of Pharmaceutical Compound in Water Matrix, Water 8 (2016) 532, https://doi.org/10.3390/w8110532.

[72] C. Hu, J.C. Yu, Z. Hao, P.K. Wong, Effects of acidity and inorganic ions on the photocatalytic degradation of different azo dyes, Appl. Catal. B Environ. 46 (2003) 35–47, https://doi.org/10.1016/S0926-3373(03)00139-5.

[73] T. Liu, K. Yin, C. Liu, J. Luo, J. Crittenden, W. Zhang, S. Luo, Q. He, Y. Deng, H. Liu, D. Zhang, The role of reactive oxygen species and carbonate radical in oxcarbazepine degradation via UV, UV/H_2O_2: Kinetics, mechanisms and toxicity evaluation, Water Res. 147 (2018) 204–213, https://doi.org/10.1016/j.watres.2018.10.007.

[75] M. Peñas-Garzón, A. Gómez-Avilés, C. Belver, J.J. Rodriguez, J. Bedia, Degradation pathways of emerging contaminants using TiO2-activated carbon heterostructures in aqueous solution under simulated solar light, Chem. Eng. J. 392 (2020), 124867, https://doi.org/10.1016/j.cej.2020.124867.

[76] R. Andreozzi, V. Caprio, R. Marotta, D. Vogna, Paracetamol oxidation from aqueous solutions by means of ozonation and H_2O_2/UV system, Water Res. 37 (2003) 993–1004, https://doi.org/10.1016/S0043-1354(02)00460-8.

[77] T.X.H. Le, T. Van Nguyen, Z. Amadou Yacouba, L. Zoungrana, F. Avril, D. L. Nguyen, E. Petit, J. Mendret, V. Bonniol, M. Bechelany, S. Lacour, G. Lesage, M. Cretin, Correlation between degradation pathway and toxicity of acetaminophen and its by-products by using the electro-Fenton process in aqueous media, Chemosphere 172 (2017) 1–9, https://doi.org/10.1016/j.chemosphere.2016.12.060.

[78] A.M. Abdel-Wahab, A.S. Al-Shirbini, O. Mohamed, O. Nasr, Photocatalytic degradation of paracetamol over magnetic flower-like TiO2/Fe2O3 core-shell nanostructures, J. Photochem. Photobiol. A Chem. 347 (2017) 186–198, https://doi.org/10.1016/j.jphotochem.2017.07.030.